

# Wind-mass transfer in S-type symbiotic binaries

## IV. Indication of high wind-mass-transfer efficiency from active phases

A. Skopal, and N. Shagatova

Astronomical Institute, Slovak Academy of Sciences, 059 60 Tatranská Lomnica, Slovakia e-mail: skopal@ta3.sk, shagatova@ta3.sk

Received / Accepted

### ABSTRACT

*Context.* Observational indications of wind-mass transfer from an evolved giant to its distant white dwarf (WD) companion in symbiotic binaries are rare. Here, we present a way to examine the neutral wind from the giant in symbiotic binaries, which is temporarily observable throughout the orbital plane during outbursts.

*Aims.* We find that the mass-loss rate from giants in the orbital plane of S-type symbiotic binaries is high, indicating a high wind-mass-transfer efficiency in these systems.

*Methods.* We modeled hydrogen column densities in the orbital plane between the observer and the WD for all suitable eclipsing S-type symbiotic binaries during outbursts in any orbital phase.

*Results.* The mass-loss rate from the giant in the orbital plane is on the order of  $10^{-6} M_{\odot} \text{ yr}^{-1}$ , which is a factor of  $\sim 10$  higher than rates derived from nebular emission produced by the ionized wind from normal giants in symbiotic stars. This finding suggests a substantial focusing of the giant's wind toward the orbital plane and, thus, its effective transfer onto the WD companion.

*Conclusions.* Our finding suggests that wind focusing on the orbital plane may be a common property of winds from giants in S-type symbiotic stars. Such wind-focusing resolves a long-standing problem of the large energetic output from their burning WDs and deficient fueling by the giant via a standard Bondi-Hoyle accretion. It also allows the WD to grow faster in mass, which lends support to the possibility that S-type symbiotic binaries are progenitors of Type Ia supernovae.

**Key words.** binaries: symbiotic – stars: mass-loss – stars: winds, outflows

### 1. Introduction

Symbiotic stars (SySts) are the widest interacting binaries; their orbital periods are typically between 1 and 3 years (for S-type systems that contain a normal giant as the donor; see Belczyński et al. 2000; Gromadzki et al. 2013) but can be significantly longer for systems that contain a Mira variable (D-type systems; Webster & Allen 1975; Hinkle et al. 2013). The accretor is a compact star, most often a white dwarf (WD). Accordingly, the large separation of their components suggests that SySts are detached binaries (e.g., Mürset & Schmid 1999), that is to say, their activity is triggered via wind-mass transfer<sup>1</sup>.

The accretion process is responsible for the WD's temperatures of  $1 - 2 \times 10^5$  K and luminosities of  $10^1 - 10^4 L_{\odot}$  (e.g., Muerset et al. 1991; Skopal 2005b). Depending on the accretion rate and the WD mass, the accreting material can either convert only its gravitational potential energy into radiation through the accretion disk and the boundary layer – the so-called accretion-powered systems<sup>2</sup> with luminosities of a few times  $10^1 L_{\odot}$  (e.g., Skopal 2005a; Mukai et al. 2016; Munari et al. 2021) – or it can also nuclearly burn on the WD surface in stable conditions, when the hydrogen-rich material is burning as it is accreting – the so-called nuclear-powered systems,<sup>3</sup> which generate luminosities of a few times  $10^3 L_{\odot}$  (e.g., Paczynski & Zytkov 1978; Shen & Bildsten 2007).

We distinguish between quiescent and active phases of SySts according to the optical light variations. During quiescent phases, the accreting WD ionizes the neighboring part of the giant's wind, giving rise to the nebular emission (e.g., Boyarchuk et al. 1966; Seaquist et al. 1984). Due to the high wind densities in the binary, the nebula is partially optically thick, which causes periodic wave-like variations in light curves as a function of the orbital phase (Skopal 2001). During active phases, unstable nuclear burning on the WD surface gives rise to transient outbursts indicated by brightening of a few magnitudes in the optical. The nuclear-powered systems can give rise to the so-called Z And-type outbursts that result from an increase in the accretion rate above that sustaining the stable burning (Skopal et al. 2017, 2020). This type of outburst shows 1–3 mag brightening(s) in the light curves on a timescale of months to years or even decades (e.g., Belyakina 1991; Brandi et al. 2005; Leibowitz & Formigini 2008; Sekeráš et al. 2019) and signs of enhanced mass outflow in the spectrum (e.g., Fernandez-Castro et al. 1995; Skopal 2006; McKeever et al. 2011). Stages with Z And-type outbursts are usually called the active phases of SySts.

During outbursts, an expanding neutral disk-like structure emerges around the burning WD in the orbital plane. Its presence, being connected exclusively with active phases, is transient (Skopal 2005b). The disk can be formed from the compression of the enhanced wind from the burning WD toward the equatorial plane due to the WD rotation (Cariková & Skopal 2012). Consequently, the disk blocks ionizing radiation from the cen-

<sup>1</sup> Roche-lobe overflow in SySts has not yet been proven; see Sect. 4.2.

<sup>2</sup> Sometimes referred to as accreting-only SySts (Munari 2019).

<sup>3</sup> Also known as shell-burning systems (e.g., Sokolowski et al. 2016).

tral burning WD in the orbital plane, which allows the giant's wind to be neutral there. This transient emergence of a neutral wind region in the orbital plane during outbursts provides us a unique opportunity to measure the  $H^0$  column densities from the observer to the WD ( $N_H^{\text{obs}}$ ) at any orbital phase of eclipsing symbiotic binaries (see Skopal 2023).

Accordingly, in this work we model the  $N_H^{\text{obs}}$  values for all suitable eclipsing SySts during active phases and around their orbit measured by Skopal (2023). Following the method of Knill et al. (1993) and Shagatova et al. (2016), we confirm the substantial focusing of the giant's wind toward the orbital plane (Sect. 2), and thus the efficient wind-mass transfer that can operate in S-type SySts (Sect. 3). We discuss our results in Sect. 4 and present our conclusions and suggestions for future work in Sect. 5.

This work is a continuation of our previous articles on the focusing of wind from the giant toward the orbital plane in S-type SySts (see Skopal & Cariková 2015, hereafter Paper I; Shagatova et al. 2016, Paper II; and Shagatova et al. 2021, Paper III). Our efforts are aimed at explaining the large mass accretion rate through the stellar wind in these systems, which is needed to explain the very high luminosities of their burning WDs (Sect. 4.1).

## 2. The method

### 2.1. Components of $N_H^{\text{obs}}$

Measured values of  $N_H^{\text{obs}}$  consist of three components. The interstellar component,  $< 2 \times 10^{21} \text{ cm}^{-2}$ , is estimated from color excesses,  $E_{B-V}$ , of the used targets (see Table 1 of Skopal 2023) according to the relationship  $N_H/E_{B-V} \sim 4.93 \times 10^{21} \text{ cm}^{-2} \text{ mag}^{-1}$  (Diplas & Savage 1994) and two circumstellar components. The latter are given by the compressed neutral wind from the WD during outbursts,  $N_H^{\text{WD}}$ , and the neutral wind from the red giant (RG),  $N_H^{\text{RG}}$ , both of which create the neutral near-orbital-plane region as described by Skopal (2023) and shown here in Fig. 1. According to the simplified model of Cariková & Skopal (2012), the  $N_H^{\text{WD}}$  component is assumed to be constant along the orbit, its value is on the order of  $10^{22} \text{ cm}^{-2}$  (from the observer to the WD's pseudo-photosphere of  $\sim 20 R_\odot$ ; see their Fig. 4), and it also includes the preignition accretion disk material. The  $N_H^{\text{RG}}$  component varies within two orders of magnitude, dominates all components, and is asymmetric with respect to the binary axis (see Fig. 1). In modeling  $N_H^{\text{obs}}$ , we neglected the interstellar component because of its relatively very small quantity, and  $N_H^{\text{WD}}$  is a variable in our modeling (see Eq. (5)).

### 2.2. Modeling $N_H^{\text{obs}}$ along the orbit

#### 2.2.1. The principle of the method

Using the equation of continuity, the theoretical value of the total hydrogen column density of the spherically symmetric wind from the giant,  $\tilde{N}_H$ , along the line of sight from the observer ( $-\infty$ ) to infinity that contains the WD,  $l$ , can be expressed as

$$\tilde{N}_H = \frac{\dot{M}}{4\pi\mu m_H} \int_{-\infty}^{\infty} \frac{dl}{r^2 v(r)}, \quad (1)$$

where  $\dot{M}$  is the mass-loss rate from the RG,  $\mu$  the mean molecular weight,  $m_H$  the mass of the hydrogen atom,  $r$  the distance from the RG center, and  $v(r)$  the wind velocity profile (WVP;

which is the velocity of the wind particles at a radial distance from the giant's center).

The form of integral (1) allows the application of the inversion method via the diagonalization of the integral operator for column density (see Knill et al. 1993). This approach yields three essential relationships (see Paper II):

1. The parameterized total hydrogen column density of the giant's wind from the inversion method can be expressed as (Dumm et al. 1999)

$$\tilde{N}_H(b) = \frac{n_1}{b} + \frac{n_K}{b^K}, \quad (2)$$

where  $n_1$ ,  $n_K$ , and  $K$  are fitting parameters, and  $b$  is the separation between the binary components,  $p$ , projected onto the plane perpendicular to the line of sight, the so-called impact parameter:  $b^2 = p^2(\cos^2 i + \sin^2 \varphi \sin^2 i)$ , where  $i$  and  $\varphi$  are the orbital inclination and the orbital phase (see Vogel 1991).

2. The WVP,

$$v(r) = \frac{v_\infty}{1 + \xi r^{1-K}}, \quad (3)$$

where  $v_\infty$  is the terminal velocity of the wind, and  $\xi = n_K \lambda_1 / n_1 \lambda_K$  is the parameter of the wind model, where  $\lambda_1 = \pi/2$  and  $\lambda_i = \lambda_1 / (i-1) \lambda_{i-1}$  ( $i \geq 2$ ) are the eigenvalues of the Abel operator (Knill et al. 1993). The parameter  $\xi$  determines the distance from the RG surface at which the wind starts to accelerate significantly, while the parameter  $K$  defines the steepness of this acceleration (see Paper II).

3. The mass-loss rate (see Shagatova et al. 2023a),

$$\dot{M} = 2\pi\mu m_H R_G \frac{n_1}{\lambda_1} v_\infty \quad (\text{g s}^{-1}). \quad (4)$$

In our approach, the asymmetric course of  $N_H^{\text{obs}}$  values relative to the binary axis (see Fig. 1) constrains two different WVPs – the ingress one within  $\varphi \sim 0.75 - 1$ , which represents the hydrogen density distribution in front of the RG orbital motion, and the egress profile within  $\varphi \sim 0 - 0.25$  resulting from the density distribution behind the RG motion. For the orbital phases between these ranges, we assumed that the velocity profile at the plane of observations changes gradually in a smooth way from the egress to the ingress profile. We used an interconnection method, which fulfills the conditions of smoothness for both the velocity profiles and the column density as functions of the orbital phase (see Shagatova & Skopal 2017). Accordingly, we calculated the column density profile of the neutral near-orbital-plane region from the observer to the WD as (see Shagatova & Skopal 2017)

$$N_H(b) = \frac{\dot{M}}{4\pi\mu m_H} \int_{-\infty}^{\pm\sqrt{p^2-b^2}} \frac{dl}{(l^2 + b^2)v(\sqrt{l^2 + b^2})} + N_H^{\text{WD}}, \quad (5)$$

where the first term on the right represents the column density of the RG wind,  $N_H^{\text{RG}}$ , while the second one,  $N_H^{\text{WD}}$ , is the contribution of the compressed neutral wind from the WD with the preignition accretion disk between the WD's warm pseudo-photosphere and the observer (see Sect. 2.1). The term  $v(\sqrt{l^2 + b^2})$  represents the egress, ingress, or transitional wind velocity, depending on the location on the line of sight and the orbital phase. The upper limit of integration corresponds to the position of the WD, where the usage of the plus or minus sign depends on the position of the binary, that is, on the angle between the line of sight and the binary axis (see

**Table 1.** Resulting parameters of modeling the  $N_{\text{H}}^{\text{obs}}$  values via function (5).

$i$	$E/I^{(a)}$	$n_1$	$n_K$	$K$	$N_{\text{H}}^{\text{WD}}$	$\dot{M}_{\text{sp}}^{(b)}$	$\chi_{\text{red}}^2$ <sup>(c)</sup>	Object	$d$	$\dot{M}$	Ref.
70°	E	9.20 <sup>+3.22</sup> <sub>-3.68</sub>	10.9 <sup>+27.3</sup> <sub>-6.5</sub>	6 <sup>+1</sup> <sub>-1</sub>	0.5 <sup>+0.9</sup> <sub>-0.5</sub>	2.84 <sup>+0.99</sup> <sub>-1.14</sub> × 10 <sup>-6</sup>	0.47	BF Cyg	3.4	< 3.3 × 10 <sup>-7(d)</sup>	(1)
	I	2.20 <sup>+1.54</sup> <sub>-1.10</sub>	15.7 <sup>+18.8</sup> <sub>-7.9</sub>	6 <sup>+1</sup> <sub>-0</sub>		6.80 <sup>+4.76</sup> <sub>-3.40</sub> × 10 <sup>-7</sup>		CI Cyg	1.6	~ 4.4 × 10 <sup>-7</sup>	(2)
80°	E	7.26 <sup>+4.36</sup> <sub>-2.54</sub>	1.33 <sup>+2.66</sup> <sub>-0.80</sub>	4 <sup>+1</sup> <sub>-1</sub>	1.0 <sup>+1.5</sup> <sub>-0.8</sub>	2.24 <sup>+1.34</sup> <sub>-0.78</sub> × 10 <sup>-6</sup>	0.35	YY Her	6.3	< 2.9 × 10 <sup>-7</sup>	(3)
	I	2.05 <sup>+2.26</sup> <sub>-1.13</sub>	3.44 <sup>+5.16</sup> <sub>-1.72</sub>	5 <sup>+1</sup> <sub>-0</sub>		6.33 <sup>+7.29</sup> <sub>-3.65</sub> × 10 <sup>-7</sup>		AR Pav	4.9	–	(4)
90°	E	3.84 <sup>+4.61</sup> <sub>-2.69</sub>	0.682 <sup>+0.750</sup> <sub>-0.341</sub>	3 <sup>+1</sup> <sub>-0</sub>	1.5 <sup>+1.5</sup> <sub>-1.2</sub>	1.19 <sup>+1.43</sup> <sub>-0.83</sub> × 10 <sup>-6</sup>	0.43	AX Per	1.7	~ 8.8 × 10 <sup>-8</sup>	(5)
	I	1.79 <sup>+2.33</sup> <sub>-1.43</sub>	1.41 <sup>+1.55</sup> <sub>-0.71</sub>	4 <sup>+1</sup> <sub>-0</sub>		5.53 <sup>+7.19</sup> <sub>-4.24</sub> × 10 <sup>-7</sup>		PU Vul	4.7	< 5.8 × 10 <sup>-7(d)</sup>	(6)

**Notes:** The first part of the table contains the fitting parameters of the wind,  $n_1$  (10<sup>23</sup> cm<sup>-2</sup>),  $n_K$  (10<sup>25</sup> cm<sup>-2</sup>),  $K$ ,  $N_{\text{H}}^{\text{WD}}$  (10<sup>22</sup> cm<sup>-2</sup>), the corresponding spherical equivalent of the mass-loss rate,  $\dot{M}_{\text{sp}}$  ( $M_{\odot}$  yr<sup>-1</sup>; see Sect. 3.1), and a minimum of the  $\chi_{\text{red}}^2$  function for three different orbital inclinations,  $i$  (see Sect. 2.2). The second part, to the right of the vertical bar, compares the total mass-loss rates,  $\dot{M}$  ( $M_{\odot}$  yr<sup>-1</sup>), derived from radio emission by Seaquist et al. (1993) recalculated for distances  $d$  (in kpc) from the literature, listed in the last column, Ref. <sup>(a)</sup> From egress (E) or ingress (I) data (see Sect. 2.2). <sup>(b)</sup> For  $v_{\infty} = 30$  km s<sup>-1</sup> (see Sect. 5.1. of Paper II). <sup>(c)</sup> Corresponds to 34 degrees of freedom. <sup>(d)</sup> Upper limit due to a contribution from the active hot component. References: (1) Muerse et al. (1991), (2) Seaquist et al. (1993), (3) Skopal (2005b), (4) Schild et al. (2001), (5) Skopal et al. (2001), and (6) Kato et al. (2012).

Shagatova & Skopal 2017 for details). For the binary parameters,  $p$  and  $R_G$ , we adopted typical values of 400  $R_{\odot}$  and 100  $R_{\odot}$ , respectively (Belczyński et al. 2000). Finally, the variables determining the model  $N_{\text{H}}(b)$  (Eq. (5)) are the  $n_1$ ,  $n_K$ , and  $K$  of the WVP (Eq. (3)), the value of  $N_{\text{H}}^{\text{WD}}$  (Sect. 2.1), and the corresponding mass-loss rate,  $\dot{M}$  (Eq. (4)).

## 2.2.2. Description of the fitting procedure

We determined the model parameters by fitting the  $N_{\text{H}}^{\text{obs}}$  values with function (5) using our own software<sup>4</sup>. To obtain the resulting parameters, we first estimated possible initial ranges of the WVP parameters  $n_1$ ,  $n_K$ , and  $K$ <sup>5</sup> while keeping  $N_{\text{H}}^{\text{WD}}$ <sup>6</sup> fixed. We iterated the following procedure:

1. We randomly generated the values of all ingress and egress WVP fitting parameters.
2. We integrated column densities (see Eq. (5)) for the corresponding WVPs using the fourth-order Runge-Kutta method.
3. We evaluated the goodness of fits via the least-square method.

Overall, we calculated 50 000 models for random WVP parameter values in the first run. Using the top 50 models, we determined their new narrower ranges. We repeated this procedure until the desired accuracy of the resulting WVP parameters (approximately a few percent) was achieved.

For the given  $N_{\text{H}}^{\text{WD}}$  and the best corresponding ingress and egress models, we compared the column densities given by Eq. (5) with the measured  $N_{\text{H}}^{\text{obs}}$  values at all orbital phases. In this way, varying the  $N_{\text{H}}^{\text{WD}}$  parameter, we selected the best solution. The resulting parameters,  $n_1$ ,  $n_K$ , and  $K$  (which define the WVP), the column density,  $N_{\text{H}}^{\text{WD}}$ , and the mass-loss rate,  $\dot{M}$ , are listed in Table 1, and Fig. 1 shows the model for  $i = 80^\circ$ .

<sup>4</sup> The Fortran codes and an application example are available at <https://zenodo.org/record/8120552>

<sup>5</sup> In the first step, we chose relatively large ranges, 10<sup>20</sup> – 10<sup>30</sup> cm<sup>-2</sup>, 10<sup>20</sup> – 10<sup>40</sup> cm<sup>-2</sup>, and 1 – 40 for the parameters  $n_1$ ,  $n_K$ , and  $K$ , respectively, to avoid missing the best solution.

<sup>6</sup> We selected  $N_{\text{H}}^{\text{WD}}$  values from the interval 0 – 10<sup>23</sup> cm<sup>-2</sup>.

Finally, we note that due to the gap in the data set around  $\varphi = 0.8$ , the least-square method did not always provide adequate values of the ingress  $n_1$  parameter. In these cases, we estimated its value so as to get a reasonable model here: For  $i = 70^\circ$ , we obtained the appropriate value of the ingress  $n_1$  parameter by fixing its value to 2.2 × 10<sup>23</sup> cm<sup>-2</sup> and performing steps 1 to 3 of the fitting procedure. For  $i = 80^\circ$ , we fixed  $n_1 = 2.05 \times 10^{23}$  cm<sup>-2</sup> and  $K = 5$ . For  $i = 90^\circ$ ; no manual intervention was needed.

## 2.2.3. Determination of uncertainties

Computing a grid of models by individually varying the values of fitting parameters around the best solutions, we estimated their uncertainties given by the errors and/or spread in  $N_{\text{H}}^{\text{obs}}$  values. Typically, these errors are large ( $\geq 50\%$  and higher), with the upper uncertainty larger than the lower. This is also true for the resulting values of the  $\dot{M}_{\text{sp}}$ , with average uncertainties at the level of ~ 50% for the lower limit and ~ 90% for the upper limit. The average value of  $\dot{M}_{\text{sp}}$  over all considered inclinations and for both the egress and ingress cases is 1.36 × 10<sup>-6</sup>  $M_{\odot}$  yr<sup>-1</sup> with a standard deviation of 9.63 × 10<sup>-7</sup>  $M_{\odot}$  yr<sup>-1</sup> (see Table 1). We also note that the uncertainty in the  $\dot{M}_{\text{sp}}$  linearly reflects the uncertainty in  $v_{\infty}$  (see Eq. (4)).

The uncertainties of the  $N_{\text{H}}^{\text{WD}}$  values are estimated from the  $N_{\text{H}}(b)$  profile around  $\varphi = 0.5$ , where the RG wind is sufficiently thin along the line of sight to allow us to identify the effect of the  $N_{\text{H}}^{\text{WD}}$  contribution. The large uncertainty of the ingress  $n_1$  parameter is directly connected to the uncertainty of the  $N_{\text{H}}^{\text{WD}}$  values shown in Table 1.

Although all the used objects are eclipsing binaries, their accurate  $i$  are not known. Therefore, we performed modeling for  $i = 90^\circ$ ,  $80^\circ$ , and  $70^\circ$  to demonstrate the effect of an uncertainty in  $i$  on the model parameters. For example, lower values of  $i$  require higher values of  $\dot{M}$  to achieve good agreement with the measured column densities. Similarly, the column density given by Eq. (2), as well as the difference between the egress and ingress data, decreases with  $i$  (Table 1). Therefore, the model requires a higher column density asymmetry in the ingress and egress orbital phases for lower  $i$ . Values of the parameter  $n_K$ , which reflects the density conditions close to the RG surface,

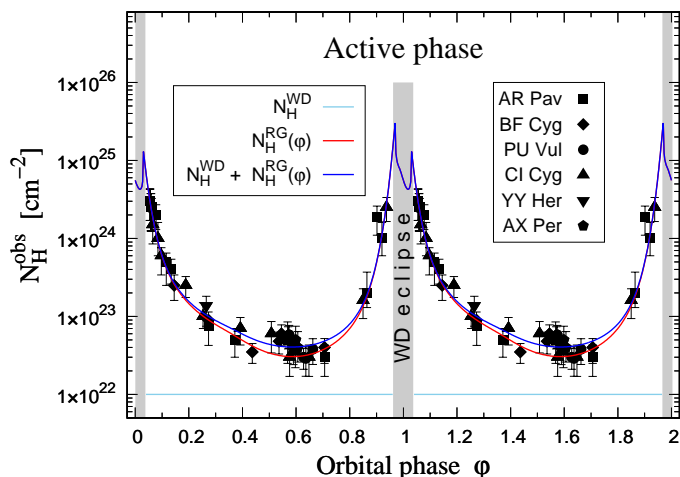


**Fig. 1.** Column densities of atomic hydrogen between the observer and the WD ( $N_{\text{H}}^{\text{obs}}$ ) measured for eclipsing SySts during active phases around the whole orbit (data from Skopal 2023). The blue line is the best-fitting model for  $i = 80^\circ$  (Table 1). It consists of a constant value along the orbit,  $N_{\text{H}}^{\text{WD}} = 1 \times 10^{22} \text{ cm}^{-2}$ , supplied by the compressed neutral wind from the WD during outbursts, and the phase-dependent value,  $N_{\text{H}}^{\text{RG}}(\varphi)$ , of the neutral wind from the RG (see Sect. 2.1). The minimum in the model during the WD eclipse is caused by the fact that the line of sight ends at the surface of the RG, and not on the warm WD’s pseudo-photosphere. Asymmetrical distribution and high values of  $N_{\text{H}}^{\text{obs}}$  reflect the asymmetric wind from the RG and its focusing on the orbital plane (see the main text).

are a strong function of  $i$ , given by the  $K$ -th power of the impact parameter  $b$  in the second term of Eq. (2). On the contrary, the values of the parameter  $n_1$ , which represents the density farther away from the RG, do not show significant variability with  $i$ . This also reflects an insignificant dependence of  $\dot{M}$  on  $i$  (see Eq. (4) and Table 1).

### 2.3. Applicability of the method

Observability of the Rayleigh scattering effect in a binary, and thus the application of our method, does not depend on the separation between the accreting WD and its donor. The method just requires the line of sight to pass through a measurable amount of the neutral wind from the giant that we can model. The ionization structure restricts the application of the method to objects with a high  $i$  (see Fig. 2f of Skopal 2023). During quiescent phases, the number of  $\text{H}^0$  atoms is measurable only around the inferior conjunction of the RG, from the observer to the  $\text{H}^0/\text{H}^+$  boundary, while during outbursts we can measure its quantity from the observer to the WD and around the whole binary. The widest symbiotic binary for which we have the required observations is PU Vul (orbital period of 13.4 years; see Shugarov et al. 2012).

## 3. Results

### 3.1. Enhanced wind-mass loss in the orbital plane

Our column density models of the neutral near-orbital-plane region (Eq. (5)) correspond to the mass-loss rate from the giant,  $\dot{M} \approx 10^{-6} M_{\odot} \text{ yr}^{-1}$  (see Table 1). However, a mass-loss rate of  $\approx 10^{-7} M_{\odot} \text{ yr}^{-1}$  has been estimated from the nebular emission of the ionized wind from the giant during quiescent phases

of S-type SySts (see Muerset et al. 1991; Seaquist et al. 1993; Mikołajewska et al. 2002a; Skopal 2005b). Because the latter approach does not depend on the line of sight (above all, it is independent of  $i$ ), the corresponding  $\dot{M}$  can be considered the total mass-loss rate.

The difference between our value of  $\approx 10^{-6} M_{\odot} \text{ yr}^{-1}$  and the total value of  $\approx 10^{-7} M_{\odot} \text{ yr}^{-1}$  may be caused by the non-spherically symmetric distribution of the particle density in the wind. In our case, using  $N_{\text{H}}^{\text{obs}}$  from the near-orbital-plane region only, we can determine only the spherical equivalent of the mass-loss rate,  $\dot{M}_{\text{sp}}$ , which assumes a spherically symmetric distribution of the particle density in the wind. If this were the case, then the equality  $\dot{M}_{\text{sp}} = \dot{M}$  would apply. Otherwise, the  $N_{\text{H}}^{\text{obs}}$  from denser parts of the wind yields  $\dot{M}_{\text{sp}} > \dot{M}$ , and vice versa. Thus, comparing the total value of the mass-loss rate with the  $\dot{M}_{\text{sp}}$  can give us important information about the density structuring of the wind. In our case of solely eclipsing systems, the line of sight pointing to their WDs always passes through the near-orbital-plane region. Therefore, our finding that  $\dot{M}_{\text{sp}} > \dot{M}$  (Table 1) implies enhanced wind-mass loss in the orbital plane. This result is consistent with that found for the quiescent SySts EG And and SY Mus (see Paper II).

### 3.2. High wind-mass-transfer efficiency

The increase in the wind-mass-loss rate in the orbital plane with the factor  $\sim \dot{M}_{\text{sp}}/\dot{M}$  implies a proportional increase in the accretion rate with respect to the spherically symmetric case. Hence, this result points to a higher efficiency of the wind-mass transfer between the binary components than what is expected for the canonical Bondi-Hoyle type of wind accretion (Bondi & Hoyle 1944). Our finding, which is derived from observations, is consistent with theoretical calculations of gravitational enhancement of the wind-mass loss in the orbital plane due to the presence of a binary companion (Frankowski & Tylenda 2001; de Val-Borro et al. 2009, 2017; Bermúdez-Bustamante et al. 2020; El Mellah et al. 2020), which can be enhanced by the compression of the wind toward the orbital plane due to the rotation of normal giants in S-type SySts (see Paper I and references therein). Also, the indication of higher  $\text{H}^0$  column densities between the binary components compared to opposite orbital phases, recently revealed for the eclipsing SySt EG And by Shagatova et al. (2023b), is likely the result of enhanced mass transfer between binary components. Here, our indication of a high wind-mass-transfer efficiency is consistent with our previous findings of the wind focusing toward the orbital plane (see Papers I, II, and III).

### 3.3. Confirmation of the wind asymmetry

Asymmetric distribution of wind particle density in the orbital plane with respect to the binary axis (see Fig. 1 and Sect. 3.3 of Skopal 2023) constrains the asymmetric WVP because the velocity of the wind determines the function for column densities (Eq. (5)). The ingress of the WVP being steeper than its egress (Eq. (3) and Table 1) implies a higher density gradient in front of the RG orbital motion than behind it. During quiescent phases, this manifests itself in the asymmetry of the ionization boundary in the orbital plane with respect to the binary axis (see Fig. 2c of Skopal 2023) and in the asymmetry of the far-UV light curves around the zero orbital phase (see Shagatova & Skopal 2017). The former is given by the asymmetric distribution of  $N_{\text{H}}^{\text{obs}}$  values around the inferior conjunction of the RG (see Fig. 2), while

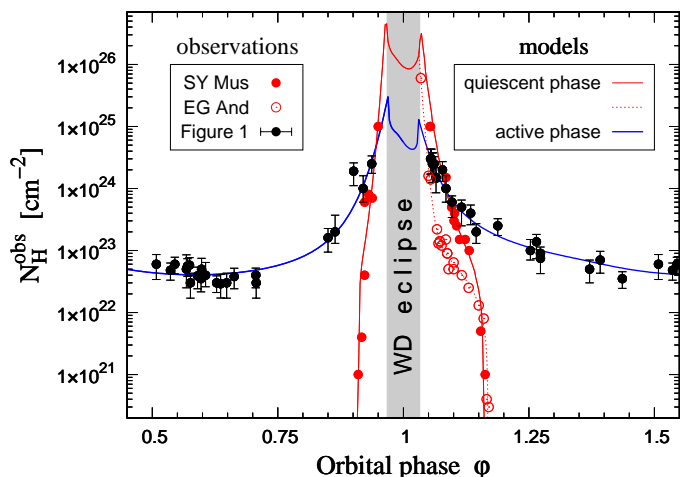


**Fig. 2.** Comparison of the  $N_{\text{H}}^{\text{obs}}$  column densities for eclipsing systems (i.e., measured in the orbital plane) during quiescent phases (red symbols; data and models from Paper II) and active phases (black circles; data and the model from Fig. 1).

the latter results from the different attenuation of the WD’s radiation along the directions in front of and behind the RG orbital motion.

As the wind asymmetry alongside the orbital motion of the RG is indicated during both the quiescent and active phases, and for different objects, this apparently represents a common feature of the wind material from normal giants in symbiotic binaries.

## 4. Discussion

### 4.1. Wind-focusing as a new mass-transfer mode in S-type SySts

The first indication of wind-focusing was suggested for the nearby SySt SS Leporis (distance of 280 parsecs, orbital period of 260 days) by interferometric measurements that resolved both binary components. The measurements revealed the RG to be almost twice smaller than its Roche lobe, which allows one to conclude that an enhanced wind-mass loss in the orbital plane fuels the abnormal luminosity of the hot component (see Blind et al. 2011). For the quiet eclipsing symbiotic systems EG And and SY Mus, we determined the wind-focusing toward the orbital plane by modeling the  $N_{\text{H}}^{\text{obs}}$  column densities around the inferior conjunction of the RG (see Paper II and our Fig. 2), which revealed a mass-loss rate in the orbital plane that is a factor of  $\sim 10$  higher than its total value. Recently, we indirectly confirmed the compression of the giant’s wind in the orbital plane for EG And by discovering significant dilution around the poles of the giant that corresponds to  $\dot{M}_{\text{sp}} \leq 10^{-8} M_{\odot} \text{ yr}^{-1}$  (see Paper III). In the present study we confirm the wind-focusing toward the orbital plane for eclipsing SySts during active phases. Wind-focusing for quiescent systems, both the accretion-powered SySt EG And and the nuclear-powered SY Mus, as well as for systems transiting the active phase, suggests that this property may be a common feature of the wind from normal giants in SySts.

The abovementioned findings indicate the presence of an efficient wind-mass-transfer mode operating in S-type SySts, especially those with nuclear shell burning, in which the high luminosity of burning WDs requires a high accretion rate. An effective wind-mass-transfer mode is a key toward resolving a

long-standing fundamental problem in SySts research: the discrepancy between the large energetic output from burning WDs and their deficient fueling by the giant in the Bondi-Hoyle type of wind accretion (first pointed by Kenyon & Gallagher 1983) because of its low efficiency<sup>7</sup> of only 0.6 to 10% (see Bondi & Hoyle 1944; Theuns et al. 1996; Nagae et al. 2004; Perets & Kenyon 2013). In particular, the high luminosities of nuclear-powered systems require a high accretion rate of  $\sim (10^{-8} - 10^{-7}) M_{\odot} \text{ yr}^{-1}$  (e.g., Paczynski & Zytlow 1978; Shen & Bildsten 2007), which cannot be fueled via the Bondi-Hoyle accretion because the mass-loss rate from RGs in S-type systems is on the same order ( $\approx 10^{-7} M_{\odot} \text{ yr}^{-1}$ ; Sect. 3.1).

Another important implication of wind-focusing is the fueling of the high-mass WDs in recurrent symbiotic novae via the wind, which also requires accretion rates of a few times  $10^{-8} M_{\odot} \text{ yr}^{-1}$  onto a  $1.25\text{--}1.40 M_{\odot}$  WD (e.g., Yaron et al. 2005; Schaefer 2009; Drake et al. 2016; Hillman & Kashi 2021).

### 4.2. Wind-focusing and ellipsoidal light variations

Due to the large separation of the binary components in SySts, the mass from the RG is expected to be transferred onto its compact companion via the stellar wind (e.g., Mürset & Schmid 1999). However, the light curves of many SySts show so-called ellipsoidal variation (i.e., two minima and two maxima per orbital cycle; see, e.g., Gromadzki et al. 2013), which is generally understood to be a result of the Roche-lobe filling giant. Therefore, this effect has been considered an indication of the mass-transfer via Roche-lobe overflow (RLOF) for symbiotic binaries (see Wilson & Vaccaro 1997; Mikołajewska et al. 2002b, 2003). However, there are a number of arguments against this natural interpretation. We summarize them as follows.

1. Modeling the corresponding optical and near-IR light curves shows that the required Roche-lobe filling factor,  $R_{\text{RG}}/R_{\text{L}}$ , is inconsistent with the cool component radii derived from measured  $v \sin(i)$  and spectral type for most systems (Rutkowski et al. 2007; Mikołajewska 2007, 2012; Otulakowska-Hypka et al. 2014).
2. The use of other methods also shows that the actual radii of RGs in SySts are too small to fill their Roche lobes. For example, (i) Vogel et al. (1992) determined the radius of an M2.4 III giant in EG And ( $P_{\text{orb}} = 482.2 \text{ d}$ ) to be only  $75 R_{\odot}$ , from the 1991 eclipse observed in the UV. (ii) Using a relation between the visual surface brightness and the Cousins  $V - I$  color index, Dumm & Schild (1998) found that radii of normal M giants increase from a median value of  $50 R_{\odot}$  at spectral type M0 III to  $170 R_{\odot}$  at M7/M8 III, for available Hipparcos parallaxes. (iii) Based on a strong correlation between the spectral type of the RG and the orbital period for 30 SySts, Mürset & Schmid (1999) found that the RG radii  $R_{\text{RG}} \leq l_1/2$  with only one exception (T CrB), where  $l_1$  is the distance from the center of the RG to the inner Lagrangian point. (iv) From the spectral energy distribution of RGs in S-type SySts and given distances, Skopal (2005b) found that their radii are far shorter than their Roche-lobe radii (see Tables 1 and 2 therein). (v) The symbiotic binary V1261 Ori shows a pronounced ellipsoidal variation in its ASAS  $V$ -band light curve, but the interferometric measurements suggest its Roche-lobe filling factor to be only  $\sim 0.3$  (see Boffin et al. 2014).
3. The largest discrepancy between the true radii of RGs and their Roche-lobe radii in symbiotic binaries is most appar-

<sup>7</sup> Defined as the mass accretion rate divided by the mass-loss rate.

ent for some yellow SySts, whose optical light curves show marked ellipsoidal variation (see Fig. 6.2 of Munari 2019), although their G-K giants with radii typically of  $30\text{--}50R_{\odot}$  are deep inside their Roche lobes.

4. Finally, our analysis also favors wind-mass transfer over RLOF because the density profile in Fig. 1 corresponds to the WVP (Eq. (3)).

The above arguments indicate that the nature of the ellipsoidal variation in the light curves of some SySts differs from that of the tidally distorted cool giants that fill their Roche lobe. Here, we propose that the substantial focusing of the wind toward the orbital plane could mimic the tidally distorted cool giants and thus produce the ellipsoidal variation in the light curves, even for systems containing RGs well within their Roche lobes. However, this idea needs further quantitative confirmation, which is beyond the scope of this paper.

#### 4.3. Comparison with D-type SySts

The efficient mass-transfer mode in D-type systems is conditioned by a slowly accelerating wind produced by a Mira-type variable with an acceleration radius that lies close to the Roche-lobe radius. In this case, the slow wind fills the Mira's Roche lobe instead of the star itself and can be effectively transferred through the  $L_1$  point to the WD – the so-called wind Roche-lobe overflow (WRLOF; see Mohamed & Podsiadlowski 2007, 2012; Abate et al. 2013). By simulating this for *o* Ceti (with a projected binary separation of  $\sim 65$  a.u. and a wind velocity of  $\approx 5 \text{ km s}^{-1}$ ), Matthews & Karovska (2006) found that the mass transfer efficiencies can be at least an order of magnitude higher than the analogous Bondi-Hoyle values. Thus, despite the large separation of the binary components, the efficiency of the mass transfer in D-type SySts is comparable with that in the S-types.

In principle, our method could also be used to examine the wind for D-type systems; however, their orbital parameters are mostly unknown, and thus there are no appropriate observations. Finally, we note that the WRLOF mode is probably not applicable to wind from normal giants in S-type SySts, which is a few times faster (Mohamed & Podsiadlowski 2007, Paper II), although proper modeling should be carried out to obtain a definitive conclusion.

## 5. Conclusion and future work

In this work we modeled the  $N_{\text{H}}^{\text{obs}}$  column densities of the wind from normal giants in eclipsing S-type SySts during their outbursts (see Sect. 1, Fig. 1, and Eq. (5)). We find that the spherical equivalent of the mass-loss rate derived from the orbital-plane column densities can be a factor of  $\approx 10$  larger than the total value (Sect. 3.1). This implies a focusing of the wind toward the orbital plane and, thus, its more efficient transfer onto the WD compared to the standard Bondi-Hoyle type of wind accretion (Sect. 3.2). Our findings independently confirm the effect of wind-focusing previously found for the quiescent SySts SY Mus and EG And and help us understand the discrepancy between the too high luminosity of H-burning WDs and their insufficient fueling through canonical Bondi-Hoyle wind accretion (Sect. 4.1).

We have several suggestions for future work. The compression of the giant's wind toward the orbital plane presents an interesting challenge for further theoretical modeling of the stellar wind morphology from giants in S-type SySts:

1. Modeling of the accretion process that meets the conditions derived from observations ( $\dot{M}_{\text{sp}}/\dot{M} \approx 10$  and  $< 0.1$  in the

orbital plane and around the poles of the RG, respectively, and a total mass-loss rate of  $\dot{M} \approx 10^{-7} M_{\odot} \text{ yr}^{-1}$ ) should more accurately determine the mass-transfer mode operating in S-type SySts (see Sect. 4.1). Also, determining the ratio of mass-loss rates,  $\dot{M}_{\text{sp}}/\dot{M}$ , as a function of  $i$  would illustrate the pole–equator asymmetry of the wind material from normal giants in SySts.

2. Consequently, the implementation of the efficient wind-mass-transfer mode in the binary population synthesis codes can improve current simulations of the birth rate and number of SySts (e.g., Lü et al. 2006).
3. Theoretical calculations of the optical depth of the compressed material in the orbital plane are needed to test whether the corresponding light curves are similar to those produced by the tidally distorted giants (see Sect. 4.2).

Finally, we note that the expected high accretion rates from the wind compressed in the orbital plane should allow the WD to grow faster in mass to the Chandrasekhar limit despite the hydrogen and helium flashes on its surface (see Hillman et al. 2016) and thus explode as a Type Ia supernova. Therefore, the wind-focusing toward the orbital plane makes S-type symbiotic binaries an effective wind-accretion channel for producing Type Ia supernovae.

*Acknowledgements.* We thank the anonymous referee for valuable comments. This work was supported by a grant of the Slovak Academy of Sciences, VEGA No. 2/0030/21, and by the Slovak Research and Development Agency under contract No. APVV-20-0148. This research has made use of NASA's Astrophysics Data System Bibliographic Services.

## References

- Abate, C., Pols, O. R., Izzard, R. G., Mohamed, S. S., & de Mink, S. E. 2013, *A&A*, 552, A26
- Belczyński, K., Mikołajewska, J., Munari, U., Ivison, R. J., & Friedjung, M. 2000, *A&AS*, 146, 407
- Belyakina, T. S. 1991, *Bulletin Crimean Astrophysical Observatory*, 83, 104
- Bermúdez-Bustamante, L. C., García-Segura, G., Steffen, W., & Sabin, L. 2020, *MNRAS*, 493, 2606
- Blind, N., Boffin, H. M. J., Berger, J. P., et al. 2011, *A&A*, 536, A55
- Boffin, H. M. J., Hillen, M., Berger, J. P., et al. 2014, *A&A*, 564, A1
- Bondi, H. & Hoyle, F. 1944, *MNRAS*, 104, 273
- Boyarchuk, A. A., Esipov, V. F., & Moroz, V. I. 1966, *Soviet Ast.*, 10, 331
- Brandt, E., Mikołajewska, J., Quiroga, C., et al. 2005, *A&A*, 440, 239
- Čariková, Z. & Skopal, A. 2012, *A&A*, 548, A21
- de Val-Borro, M., Karovska, M., & Sasselov, D. 2009, *ApJ*, 700, 1148
- de Val-Borro, M., Karovska, M., Sasselov, D. D., & Stone, J. M. 2017, *MNRAS*, 468, 3408
- Diplas, A. & Savage, B. D. 1994, *ApJ*, 427, 274
- Drake, J. J., Delgado, L., Laming, J. M., et al. 2016, *ApJ*, 825, 95
- Dumm, T. & Schild, H. 1998, *New A*, 3, 137
- Dumm, T., Schmutz, W., Schild, H., & Nussbaumer, H. 1999, *A&A*, 349, 169
- El Mellah, I., Bolte, J., Decin, L., Homan, W., & Keppens, R. 2020, *A&A*, 637, A91
- Fernandez-Castro, T., Gonzalez-Riestra, R., Cassatella, A., Taylor, A. R., & Seauquist, E. R. 1995, *ApJ*, 442, 366
- Frankowski, A. & Tylenda, R. 2001, *A&A*, 367, 513
- Gromadzki, M., Mikołajewska, J., & Soszyński, I. 2013, *Acta Astron.*, 63, 405
- Hillman, Y. & Kashi, A. 2021, *MNRAS*, 501, 201
- Hillman, Y., Prialnik, D., Kovetz, A., & Shara, M. M. 2016, *ApJ*, 819, 168
- Hinkle, K. H., Fekel, F. C., Joyce, R. R., & Wood, P. 2013, *ApJ*, 770, 28
- Kato, M., Mikołajewska, J., & Hachisu, I. 2012, *ApJ*, 750, 5
- Kenyon, S. J. & Gallagher, J. S. 1983, *AJ*, 88, 666
- Knill, O., Dgani, R., & Vogel, M. 1993, *A&A*, 274, 1002
- Leibowitz, E. M. & Formiggini, L. 2008, *MNRAS*, 385, 445
- Lü, G., Yungelson, L., & Han, Z. 2006, *MNRAS*, 372, 1389
- Matthews, L. D. & Karovska, M. 2006, *ApJ*, 637, L49
- McKeever, J., Lutz, J., Wallerstein, G., Munari, U., & Siviero, A. 2011, *PASP*, 123, 1062
- Mikołajewska, J. 2007, *Baltic Astronomy*, 16, 1
- Mikołajewska, J. 2012, *Baltic Astronomy*, 21, 5

- Mikolajewska, J., Ivison, R. J., & Omont, A. 2002a, *Advances in Space Research*, 30, 2045
- Mikolajewska, J., Kolotilov, E. A., Shugarov, S. Y., Tatarnikova, A. A., & Yudin, B. F. 2003, in *Astronomical Society of the Pacific Conference Series*, Vol. 303, *Symbiotic Stars Probing Stellar Evolution*, ed. R. L. M. Corradi, J. Mikolajewska, & T. J. Mahoney, 151
- Mikolajewska, J., Kolotilov, E. A., Shugarov, S. Y., & Yudin, B. F. 2002b, *A&A*, 392, 197
- Mohamed, S. & Podsiadlowski, P. 2007, *Astronomical Society of the Pacific Conference Series*, Vol. 372, *Wind Roche-Lobe Overflow: a New Mass-Transfer Mode for Wide Binaries*, ed. R. Napiwotzki & M. R. Burleigh, 397
- Mohamed, S. & Podsiadlowski, P. 2012, *Baltic Astronomy*, 21, 88
- Muerstet, U., Nussbaumer, H., Schmid, H. M., & Vogel, M. 1991, *A&A*, 248, 458
- Mukai, K., Luna, G. J. M., Cusumano, G., et al. 2016, *MNRAS*, 461, L1
- Munari, U. 2019, arXiv e-prints, arXiv:1909.01389
- Munari, U., Traven, G., Masetti, N., et al. 2021, *MNRAS*, 505, 6121
- Mürset, U. & Schmid, H. M. 1999, *A&AS*, 137, 473
- Nagae, T., Oka, K., Matsuda, T., et al. 2004, *A&A*, 419, 335
- Otulakowska-Hypka, M., Mikolajewska, J., & Whitelock, P. A. 2014, in *Astronomical Society of the Pacific Conference Series*, Vol. 490, *Stellar Novae: Past and Future Decades*, ed. P. A. Woudt & V. A. R. M. Ribeiro, 367
- Paczynski, B. & Zytkov, A. N. 1978, *ApJ*, 222, 604
- Perets, H. B. & Kenyon, S. J. 2013, *ApJ*, 764, 169
- Rutkowski, A., Mikolajewska, J., & Whitelock, P. A. 2007, *Baltic Astronomy*, 16, 49
- Schaefer, B. E. 2009, *ApJ*, 697, 721
- Schild, H., Dumm, T., Mürset, U., et al. 2001, *A&A*, 366, 972
- Seaquist, E. R., Krogulec, M., & Taylor, A. R. 1993, *ApJ*, 410, 260
- Seaquist, E. R., Taylor, A. R., & Button, S. 1984, *ApJ*, 284, 202
- Sekeráš, M., Skopal, A., Shugarov, S., et al. 2019, *Contributions of the Astronomical Observatory Skalnaté Pleso*, 49, 19
- Shagatova, N. & Skopal, A. 2017, *A&A*, 602, A71
- Shagatova, N., Skopal, A., & Cariková, Z. 2016, *A&A*, 588, A83 (Paper II)
- Shagatova, N., Skopal, A., & Cariková, Z. 2023a, *A&A*, 676, C3
- Shagatova, N., Skopal, A., Kundra, E., et al. 2023b, *A&A*, 676, A98
- Shagatova, N., Skopal, A., Shugarov, S. Y., et al. 2021, *A&A*, 646, A116 (Paper III)
- Shen, K. J. & Bildsten, L. 2007, *ApJ*, 660, 1444
- Shugarov, S., Chochol, D., & Kolotilov, E. 2012, *Baltic Astronomy*, 21, 150
- Skopal, A. 2001, *A&A*, 366, 157
- Skopal, A. 2005a, in *Astronomical Society of the Pacific Conference Series*, Vol. 330, *The Astrophysics of Cataclysmic Variables and Related Objects*, ed. J. M. Hameury & J. P. Lasota, 463
- Skopal, A. 2005b, *A&A*, 440, 995
- Skopal, A. 2006, *A&A*, 457, 1003
- Skopal, A. 2023, *AJ*, 165, 258
- Skopal, A. & Cariková, Z. 2015, *A&A*, 573, A8 (Paper I)
- Skopal, A., Shugarov, S. Y., Munari, U., et al. 2020, *A&A*, 636, A77
- Skopal, A., Shugarov, S. Y., Sekeráš, M., et al. 2017, *A&A*, 604, A48
- Skopal, A., Teodorani, M., Errico, L., et al. 2001, *A&A*, 367, 199
- Sokoloski, J., Lawrence, S., Crots, A. P. S., & Mukai, K. 2016, in *Accretion Processes in Cosmic Sources*, 21
- Theuns, T., Boffin, H. M. J., & Jorissen, A. 1996, *MNRAS*, 280, 1264
- Vogel, M. 1991, *A&A*, 249, 173
- Vogel, M., Nussbaumer, H., & Monier, R. 1992, *A&A*, 260, 156
- Webster, B. L. & Allen, D. A. 1975, *MNRAS*, 171, 171
- Wilson, R. E. & Vaccaro, T. R. 1997, *MNRAS*, 291, 54
- Yaron, O., Prialnik, D., Shara, M. M., & Kovetz, A. 2005, *ApJ*, 623, 398